Practical considerations for the design of an aeroelastic energy harvester

Practical considerations for the design of an aeroelastic energy harvester

motion from structural vibrations and dynamic aeroelastic instabilities are possible sources of kinetic energy that can be converted to electrical energy. De Marqui et al. [2] performed a study in frequency domain, showing the effect over the flutter response of a piezoelectric plate. Bryant et al. [3] investigated the flutter response of a piezoelectric wing and the amount of energy harvested from post-flutter LCOs, due to the introduction into the model of nonlinearities, coming from the dynamic stall model. The extraction of energy from turbulence induced oscillation was the object of attention of many researchers. Akaydin et al. [4] proposed a piezoelectric beam which is able to generate electric energy from the vibrations induced by a turbulent flow at high Reynolds number. Abdelkefi et al. [5] investigated the possibility to harvest energy from transverse galloping oscillations in frequency domain and for different cross-section geometries of the chosen bluff-body. De Marqui Jr. et al. [6] modeled a piezoelectric wing generator with continuous and segmented electrodes for the purpose of energy harvesting from a discrete gust. Bryant et al. [7] presented an interesting design for power generation from aeroelastic vibrations; consisting of a simple wing pin connected to the tips of a pair of bimorph piezoelectric beams. The objective of this manuscript is to investigate a suitable design approach of a piezoelectric wing for energy extraction from aeroelastic induced vibrations. Section 2 introduces the mathematical model of the piezoelectric wing, implemented, in Matlab/Simulink®, to perform numerical analyses. The final layout of the experimental piezoelectric wing was extracted from a numerical procedure based on the identification of a set of dimensionless design parameters, Section 3. The wing, partially manufactured via a 3D printer, was tested first at the shaker, to identify its modal response and verify the consistency between experimental and numerical models, and then at the wind tunnel to experience aeroelastic instabilities. The amount of energy extracted from aeroelastic induced vibrations was evaluated for different configuration of the piezoelectric elements bonded over the wing primary structure.

2. MATHEMATICAL MODEL

The study presented in the following sections referring to the nonlinear dynamical behaviour of a slender piezoelectric wing, rely on the derivation of the nonlinear equations of motions according to the assumptions of the 3D Euler-Bernoulli beam [8],[9],[10],[11] and the Wagner representation of the unsteady aerodynamic loads [12], [13]. Figure 1 shows two reference frames: a fixed frame XYZ and a local frame $\xi\eta\zeta$, which follows the wing cross section, which are defined to derive the equations of motion.

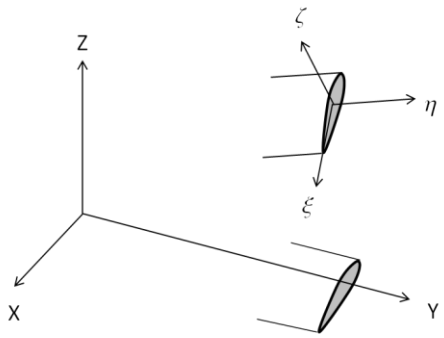

Figure 1: Reference frames.

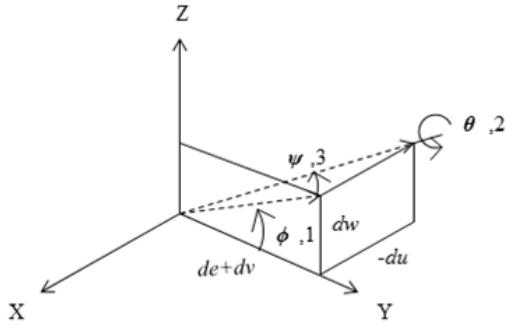

Figure 2: Euler angles and displacements derivatives.

The displacement components, $u[y,t], v[y,t], w[y,t]$ along the inertial axis, XYZ, and the Euler angles, ϕ, ψ, θ, which provide the link between the two previous mentioned reference frames, are reported in Figure 2. The application to the piezoelectric wing model of the extended Hamilton principle first and of the Galerkin approximation after, leads to a set of equations as those hereafter stated in their state space form [14],[15]:

$$\{\dot{z}\} = [S]\{z\} + [N] + \{B\} \tag{1}$$

$\{z\} = \{\dot{r} \quad r \quad V \quad w_1 \quad \cdots \quad w_4\}^T$ is the state vector, and $\{r\} = \{r_{\theta_i} \quad \cdots \quad r_{\theta_n} \quad r_{w_i} \quad \cdots \quad r_{w_n} \quad r_{u_i} \quad \cdots \quad r_{u_n}\}^T$ is the vector of the generalized coordinates, which comes from the decomposition of the displacements vector into the product of a time dependent component and of a spatial dependent component, as shown in Equation (2):

$$\begin{Bmatrix} \theta \\ w \\ u \end{Bmatrix} = [\Phi(y)]\{r(t)\} = \begin{bmatrix} \phi_{\theta_1} & \cdots & \phi_{\theta_n} & 0 & \cdots & 0 & 0 & \cdots & 0 \\ 0 & \cdots & 0 & \phi_{w_1} & \cdots & \phi_{w_n} & 0 & \cdots & 0 \\ 0 & \cdots & 0 & 0 & \cdots & 0 & \phi_{u_1} & \cdots & \phi_{u_n} \end{bmatrix} \begin{Bmatrix} r_{\theta_1} \\ \vdots \\ r_{\theta_n} \\ r_{w_1} \\ \vdots \\ r_{w_n} \\ r_{u_1} \\ \vdots \\ r_{u_n} \end{Bmatrix} \tag{2}$$

The matrix $[S]$ of Equation (1) can be written in terms of the system generalized matrices as follows:

$$[S] = \begin{bmatrix} -[M]^{-1}[D] & -[M]^{-1}[K] & [M]^{-1}[\Xi] & -[M]^{-1}[W] \\ I & 0 & 0 & 0 \\ -[\Xi]^T {C_p}^{-1} & 0 & -\left(R_{eq} \cdot C_p\right)^{-1} & 0 \\ 0 & & [W_0] & \end{bmatrix} \tag{3}$$

where $[M], [K], [D]$ represent the generalized mass matrix, the generalized stiffness matrix and the generalized damping matrix, respectively, and each of them contains both linear and nonlinear

terms, coming from the assumption of geometric nonlinearities up to the third order. $R_{eq} = 2 \cdot R$ is instead the equivalent resistance of the two electric circuits coupled to the piezoelectric patches. In addition, $[\Xi] = \begin{bmatrix} 0 \\ N_{14} \int_0^l \phi_w \frac{d^2 H}{d_y{}^2} dy \\ 0 \end{bmatrix}$ represents the electromechanical coupling vector [7], and C_p the piezoelectric capacitance, while $[W]$ and $[W_0]$ are two linear matrix depending of the constant terms of the Wagner function. $[N]$ is a linear matrix containing the first time derivative of the Wagner's function, and $\{B\} = \{M_e \quad L_e \quad 0 \quad 0 \quad ... \quad 0\}^T$ is the vector of the loads due to the trimmed condition. This set of equations, implemented and solved using Matlab/Simulink®, allows for the analysis of the aeroelastic response and of the energy harvested from it, under the assumptions of a piezoelectric wing which undergoes small elastic perturbations and moderate to large static deflections. Two modes per each degree of freedom have been assumed for numerical simulations. The results coming from the numerical model, together with the experimental results, are presented into the next chapters.

3. NUMERICAL AND EXPERIMENTAL RESULTS

The principal objective of this work is to experimentally investigate the advantages derived from a piezoelectric wing configuration, in terms of energy harvesting. Secondly, the study also intends to assess the vibration damping performance of such piezoelectric wing. In order to accomplish these objectives, it is mandatory to well identify all the initial design constraints that may come from the design methods as well as from the test facilities. The experimental test campaign was entirely performed at Clarkson University (CU). Clarkson's high-speed wind tunnel has a test section of 122×91.5×152.4 cm, and a contraction ratio of the preceding nozzle of 8:1.

Wind tunnel parameters, such as the maximum measurable speed in the available test chamber, 70 m/s, represent the main constraints which drive the design of the experimental piezoelectric wing. Therefore, in order to experience flutter vibrations, or aeroelastic instabilities in general, it is mandatory to build a wing prototype, with certain structural and geometrical characteristics, which behaves within the mentioned infrastructural limits. The section "Wind Tunnel Slender Wing Parametric Design", proposes a sensitivity study based on the frequency response of the mathematical model, illustrated in the previous chapter, in order to identify the most appropriate set of dimensionless wing parameters to be used as the baseline for the design of the experimental wing. Once these suitable wing parameters have been identified and the final piezoelectric layout has been selected, the test campaign is launched. In the section "Experimental Model Manufacturing and Test Apparatus" are provided all the details regarding the wing manufacturing and the test facilities, while section "Shaker Tests and Wind Tunnel Tests" contains the results of the experimental test and the comparisons with those generated form the numerical model.

3.1 Wind Tunnel Slender Wing Parametric Design

In order to identify the wing structural and geometrical characteristics that guarantee the desired flutter conditions, a set of dimensionless parameters were chosen based on experience and on a sensitivity study considering: i) the position of the gravity center, $\zeta_x = \frac{x_a}{b}$, ii) the location of the

elastic axis, a, and iii) the bending to torsional stiffness ratio, $\frac{EI_x}{GJ_t}$. These three parameters commonly represent the main source of uncertainty when comparing numerical with the experimental results. The effects over the flutter speed of $\zeta_x = \frac{x_a}{b}$, a and $\frac{EI_x}{GJ_t}$, are presented in Figures 3, 4 and 5, where a significant reduction of the flutter speed is achieved by increasing, one by one, the initial values of the parameters a, x_a and $\frac{EI_x}{GJ_t}$. The initial values of a, x_a and $\frac{EI_x}{GJ_t}$ were chosen from the merging between the results of a previous study performed by the authors in the same wind tunnel on a slender wing and the trial and error results from the numerical model. These values are: $\frac{EI_x}{GJ_t} = 0.52\,, a = -0.28, x_a = 0.00527\ m$.

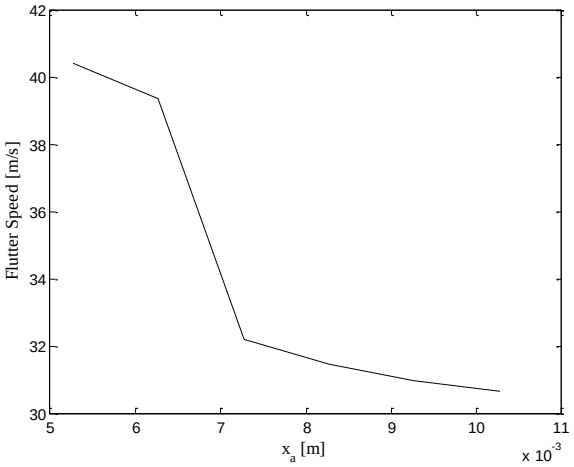

Figure 3: Flutter speed vs. center of gravity position w.r.t. the elastic axis in the chord direction.
$\frac{\mathrm{EI_x}}{\mathrm{GJ_t}} = 0.52\,, \mathrm{a} = -0.28$

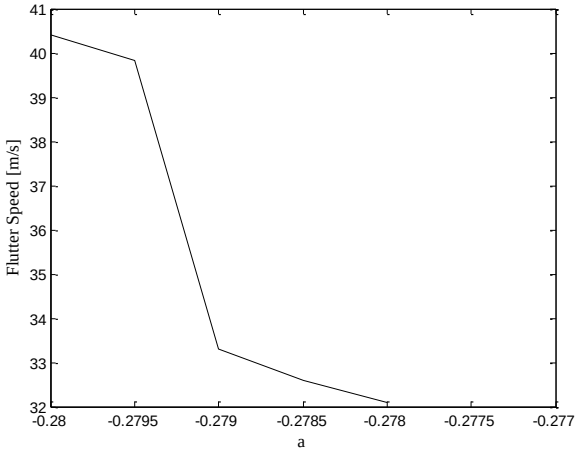

Figure 4: Flutter speed vs. shear center position, normalized by the half chord, w.r.t. the mid-chord.
$\frac{\mathrm{EI_x}}{\mathrm{GJ_t}} = 0.52\,, \mathrm{x_a} = 0.00527$ m.

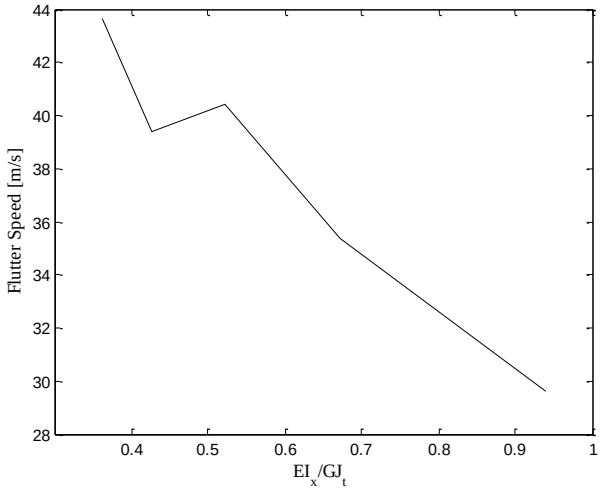

Figure 5: Flutter speed vs. Torsional stiffness per unitary length.
$\mathrm{x_a} = 0.00527$ m, $\mathrm{a} = -0.28$.

From Figures 3 through 5, a suitable flutter speed can be identified. By assuming the elastic axis position with respect to the mid-chord a = -0.28, the stiffness ratio, $\frac{EI_x}{GJ_t}$ = 0.52, and the gravity center position, x_a = 0.00727 m, the flutter speed has an estimated to be 32.18 m/s. The equivalent study has been performed on the first three modal frequencies and on the flutter frequency, as shown in Figures 6 through 8.

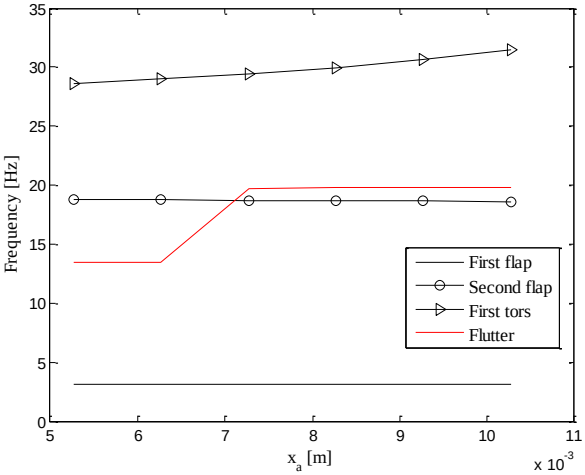

Figure 6: Flutter frequency vs. center of gravity position w.r.t. the elastic axis in the chord direction. $\frac{\mathrm{EI_x}}{\mathrm{GJ_t}} = 0.52$, $\mathrm{a} = -0.28$.

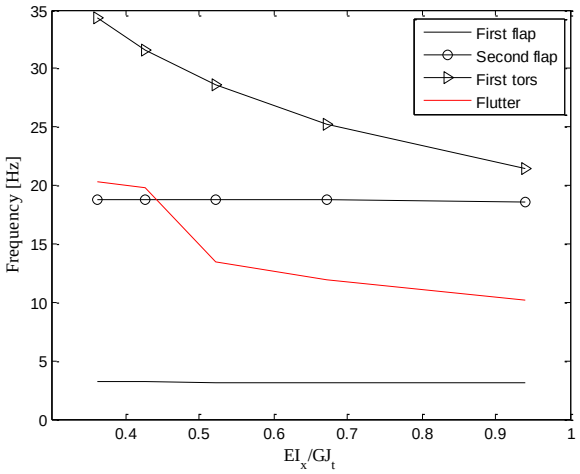

Figure 7: Frequency vs. Torsional stiffness per unitary length. $\mathrm{x_a} = 0.00527$ m, $\mathrm{a} = -0.28$.

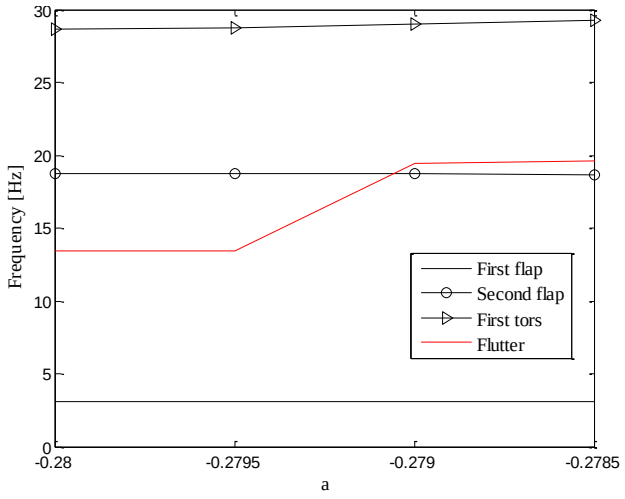

Figure 8: Frequency vs. shear center position, normalized by the half chord, w.r.t. the mid-chord. $\frac{\mathrm{EI_x}}{\mathrm{GJ_t}} = 0.52$, $\mathrm{x_a} = 0.00527$ m.

By maintaining the previously selected parameters' value, that's to say: a equal to -0.28, the stiffness ratio, $\frac{\mathrm{EI_x}}{\mathrm{GJ_t}}$, equal to 0.52 and the gravity center position, $\mathrm{x_a}$, equal to 0.00727 m, the flutter frequency is equal to 19.78 Hz, Figures from 6 to 8. The non-dimensional values of the piezoelectric wing cross-section, Figure 7, resulting from the sensitivity study are summarized in Table 1.

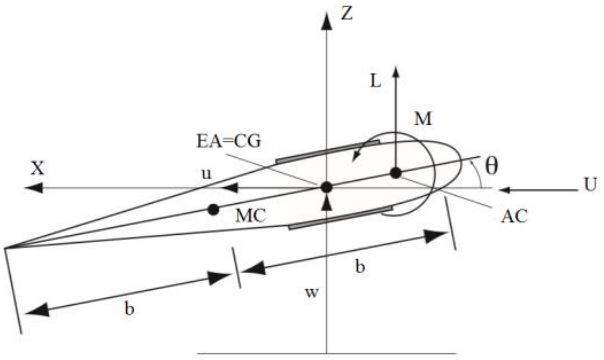

Figure 9: Piezoelectric wing cross-section.

k	λ	μ	Γ	Θ	ζ_x	ζ_z	r^2	a
$\frac{\omega b}{U}$	$\frac{L}{b}$	$\frac{m}{\pi\rho b^2}$	$\frac{EI_z}{EI_x}$	$\frac{EI_x}{GJ_t}$	$\frac{x_a}{b}$	$\frac{y_a}{b}$	$\frac{I_p}{mb^2}$	-
-	7.8	76.3	10	0.52	0.16	0	0.25	-0.28

Table 1: Non-dimensional wing cross sectional parameters

In Table 1 *k* represents the reduced frequency, λ is the wing aspect ratio, and μ is the reduced mass. In addition, Γ is the ratio between the in-plan and the out of plane bending stiffness, Θ the ratio between the out of plane banding stiffness and the torsional stiffness, ζ_x and ζ_z are the gravity center offset with respect to the elastic axis, respectively. Finally, r^2 is the square of the radius of gyration. A torque-tube [16] solution based on the structural decoupling between the bending and the torsional stiffness is adopted to ease the design of a piezoelectric wing with global characteristics as in Table 1. While the bending stiffness is entrusted to the spars, the torsion stiffness comes from the spars' connection elements, which, for the sake of the functional optimization, are modelled as NACA 0012 wing profiles. Figure 10 reproduces the wing Patran® model based on the previous assumptions.

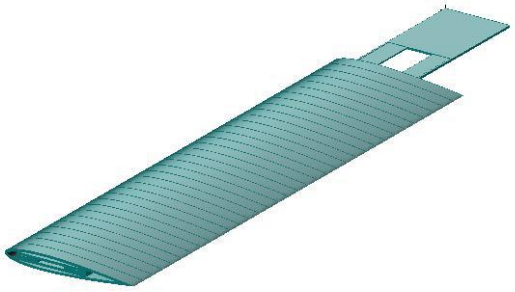

Figure 10: Wing layout with spar.

The total length of the wing is 0.35 m, covered by 34 slices, NACA 0012, of 10 mm thick each, which are not anchored to the spars surface except for the last one, the wing tip slice, which is assumed perfectly bonded on it in order to avoid the remaining to slip off. The FEM considers all details from the manufacturing and testing, such as the slits over the spars surfaces for the

piezoelectric patches placement and a plane strip at the tip of both spars to allow the last slice to glue on, Figure 11.

Figure 11: Spar detail, orange indicates placement of piezoelectric patches.

The spars are made of a standard aluminium alloy, to guarantee a good flexibility, a low transverse thickness and a good surface for the bonding of the piezoelectric elements. The slices are instead made of Poly-Lactic Acid (PLA) plastic, manufactured via a 3-D printer. The piezoelectric patches, bonded over the spars, are micro fiber composites (MFC) and cover half of the spars length. In order to perform the FEM analysis, different types of meshes were used for each component, according to the geometry and the function of the components. Solid elements HEXA 8 were used for the spar, QUAD 4 elements for the MFCs components, and TETRA 10 for the slices. Figure 12 reports some details of the spars and of the tip slice, according to the mentioned mesh types.

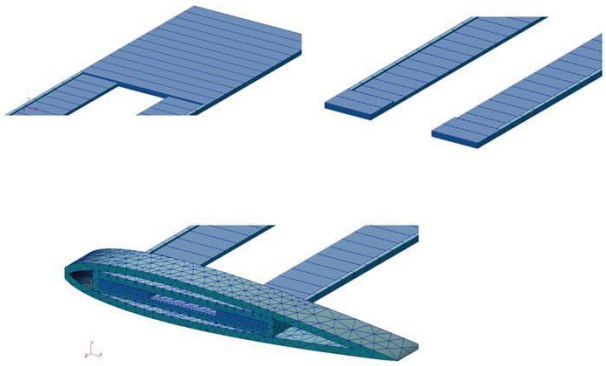

Figure 12: Mesh type for the wing's components.

The model is based on the set of non-dimensional wing parameters presented in Table 1. Table 2 contains all the geometrical and structural details of the piezoelectric wing as by CAD derivation.
Figure 13 shows the comparison between the nonlinear behaviour of the numerical model defined in Chapter 2 and the FEM model, defined in this chapter. The frequency of the first three modes is derived by assuming a variable static deformation of the wing tip as percentage of the half-wing span.

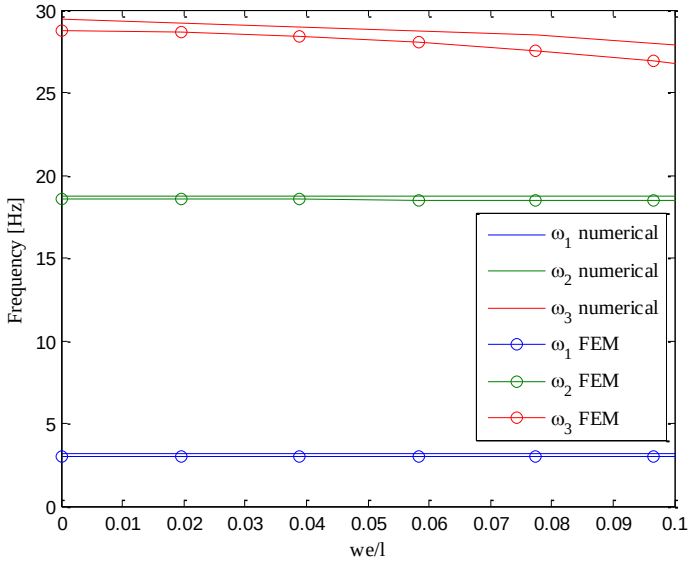

Figure 13 : Wing proper frequencies evolution for various wing tip static deflections.

Length	$\boldsymbol{L}$	$0.35\,m$
Chord	$\boldsymbol{c}$	$0.09\,m$
Wing total mass	$\boldsymbol{m}$	$212 * 10^{-3}\,Kg$
Polar moment of inertia	$\boldsymbol{I}$	$1.032 * 10^{-4}\,Kg * m^2$
Position of the gravity center in X direction	$\boldsymbol{X_{cg}}$	$7.27 * 10^{-3}\,m$
Position of the gravity center in Y direction	$\boldsymbol{Y_{cg}}$	$-0.022 * 10^{-3}\,m$
Position of the gravity center in Z direction	$\boldsymbol{Z_{cg}}$	$177.9 * 10^{-3}\,m$
Elastic modulus aluminium	$\boldsymbol{E_A}$	$71\,GPa$
Poisson ratio aluminium	$\boldsymbol{\nu_A}$	0.33
Elastic modulus PLA	$\boldsymbol{E_{PLA}}$	$1.4\,GPa$
Poisson ratio PLA	$\boldsymbol{\nu_{PLA}}$	0.35
Piezoelectric constant	$\mathbf{d_{31}}$	$-2.1 * 10^2\ pC/N$
Elastic modulus of the MFC	$\boldsymbol{E_p}$	$30.336\,GPa$
Capacitance	$\mathbf{C_p}$	$91\ nF$
MFC active length	$\mathbf{l_p}$	$0.17\ m$
MFC active width	$\mathbf{s_p}$	$0.007\ m$
MFC thickness	$\mathbf{t_p}$	$0.0003\ m$
MFC total mass	$\mathbf{m_p}$	$0.00388\ Kg$

Table 2: Piezoelectric wing values

The results of Figure 13 show a good agreement between the two wing models, allowing to allow moving from the conceptual study of the wing to its manufacturing. The wing manufacturing and the test campaign are presented and discussed in the next chapters.

3.2 Experimental Wing Model Manufacturing and Test Apparatus

The data provided in Table 2 were assumed as the reference values for the manufacturing of the piezoelectric wing to be tested. Thirty-four slices, each of them one millimetre thick, were used to cover the spars length. The slices were produced in PLA via Fused Deposition Modelling (FDM) Technique. The wing spars instead were simply machined out of a standard Aluminium alloy bar at the automatic machining center *Sharp Model SV-2412 Mini Mill* by the company *Action Machinery Co*. Due to the PLA material dilatation, during the solidification phase, several specimens of the wing slices were produced, by correcting the 3-D printing setting, before getting the desired extruded wing body. The MFC piezoelectric components, provided by Smart Material Corporation [17], consist of rectangular piezoelectric rods sandwiched between layers of adhesive, electrodes and polyimide films.

The high speed wind tunnel, used for the test campaign, can reach a maximum speed in the test chamber of 70 m/s. A proper calibration test of the wind tunnel was performed before the beginning of the experimental test, in order to avoid any undesired result. The maximum speed variation measured in the testing chamber was lower than 0.5 m/s and the turbulence level quite negligible. The flow speed, in the testing chamber, is evaluated through a classical Pitot tube, installed upstream, and connected to a digital pressure transducer. Figure 14 shows some of the test equipment's. The interaction between the wind tunnel test equipment and the piezoelectric wing is reproduced in Figure 15. The piezoelectric elements, bonded over the wing spars, are connected to two separated purely resistive electric circuits and the voltage across the resistive load is measured trough an oscilloscope. The displacements of the wing tip are measured through a laser vibrometer, who extract the velocity data of 25 scanning points placed over the outer wing surface. In order to make this data extraction easier, five stripes of reflecting material are glued beneath the scanning points.

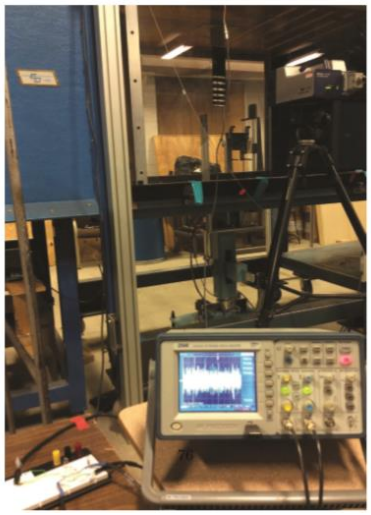

Figure 14: Wind Tunnel tests setup.

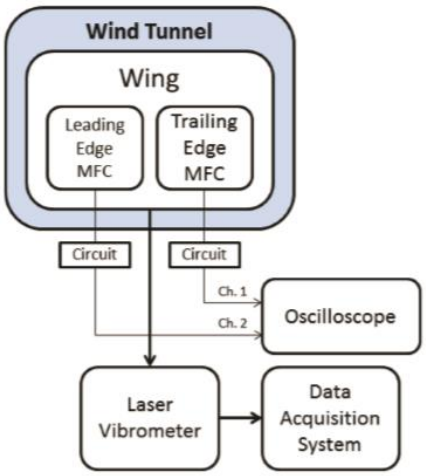

Figure 15: Shunting scheme of the piezoelectric wing.

The experimental test campaign also included the modal tests performed at the shaker, in order to extract the dynamical characteristic of the wing and to compare these with those obtained from the numerical analysis. Figure 16 shows the connections between the systems, (a), and the wing set up, (b), during the shaker tests. In order to properly transmit the load from the shaker to the wing, the spars length has been increased of 5 cm from the clamped edge. This extra surface is used as the plane support over which the stringer acts to transmit the loads generated by the signal generator. The load is applied in the proximity of the wing root, where the displacements field is very small, so a continuous contact between the wing surface and the stringer is always guaranteed, and so far from the first beam vibration nodes.

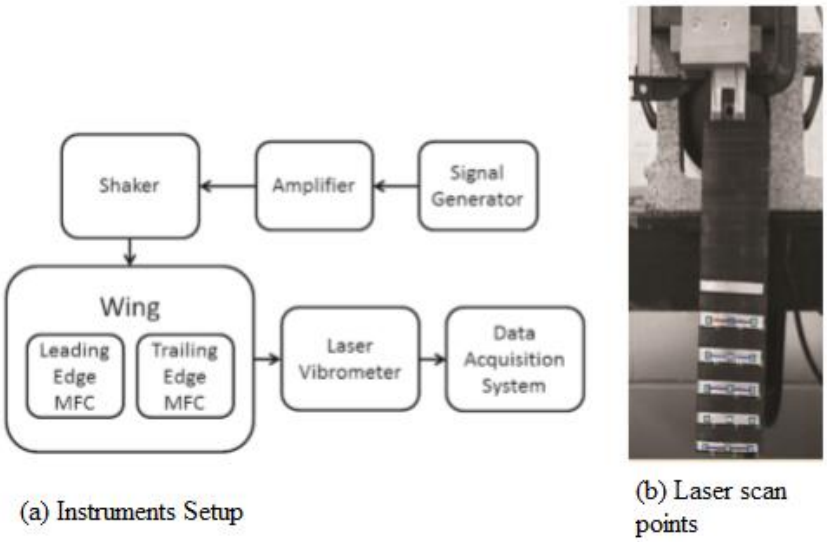

Figure 16: (a) Signal generation and propagation scheme, (b) Wing set up during shaker tests.

3.3 Shaker Test and Wind Tunnel Test

The modal shaker test consists in exciting the wing, with a sinusoidal load, at a frequency, as close as possible, to the structure resonant frequency, in order to reduce the applied load amplitude. The analytical representation of the shaker test model is synthesized in equation (4).

$$\{\dot{z}\} = [S]\{z\} + [N]\{z(0)\} + \{F_{shaker}\} \tag{4}$$

Where the load applied by the stringer of the shaker to the wing is modelled by equation (5), where A is the amplitude of the sinusoidal load and $\delta(y - 0.02)$ is the Dirac function which define the external load application point.

$$\{F_{shaker}\} = \begin{Bmatrix} 0 \\ 0 \\ \int_0^l \phi_{w1}(y)\delta(y-0.02) * A\sin(\omega_i t)\, dy \\ \int_0^l \phi_{w2}(y)\delta(y-0.02) * A\sin(\omega_i t)\, dy \\ 0 \\ 0 \end{Bmatrix} \quad (5)$$

During the tests, in both the shaker than wind tunnel, a resistive circuit was constructed on a breadboard and the output signal recorded by an oscilloscope, as shown in Figure 17.

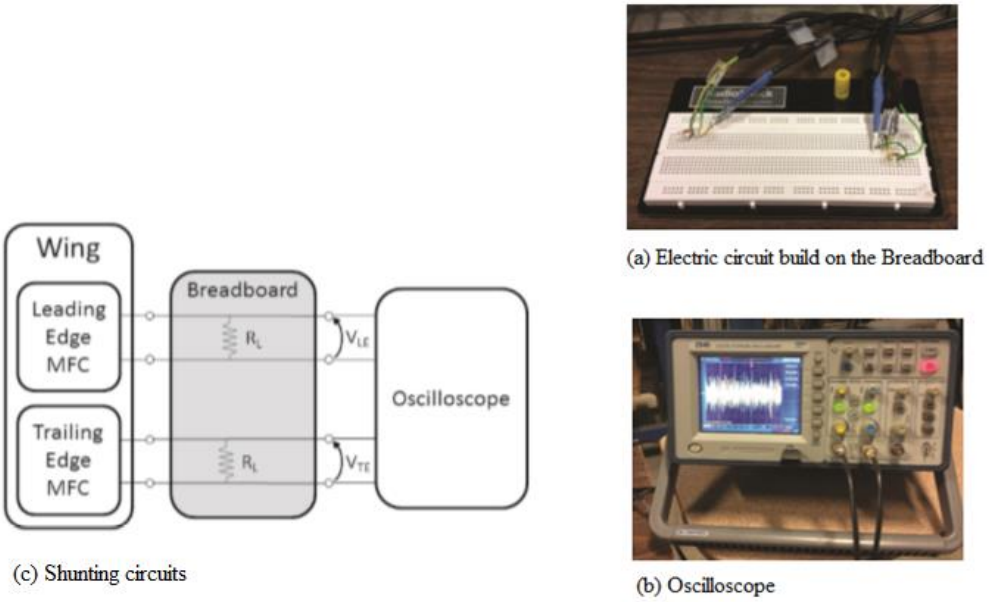

Figure 17: Test configuration of the piezoelectric circuit.

The electrical resistance was assumed equal to $10^8\ \Omega$, equivalent to the open circuit condition. Next, an impulse force was then applied by the shaker head, in order to identify the resonance frequencies of the first three modes. Table 3 shows the comparison between the values obtained from the numerical Matlab ® code, built on the model analytical representation of Chapter 2, and the experimental results of the shaker tests.

Modal shaker test configuration			
	First bending $R = 10^8\ \Omega$	**Second bending $R = 10^8\ \Omega$**	**First Torsion $R = 10^8\ \Omega$**
Experimental	2.563 Hz	14.72 Hz	21.44 Hz
Numerical	2.48 Hz	15.09 Hz	26.01 Hz

Table 3: Resonant frequencies of the piezoelectric wing configuration.

The values of the first two bending frequencies of Table 3, which show a good agreement between the numerical and the experimental models, were used to perform the energy harvesting test from

modal excitation. These values were kept constant during the whole test phase, while the resistive load varied in a range between 10^3 Ω to 10^7 Ω. The power extracted, in both experimental than numerical simulations, was calculated according to equation (6).

$$\text{Power} = \frac{{V_{RMS}}^2}{R} \tag{6}$$

Where for a sinusoidal signal $V_{RMS} = \frac{V_{peak}}{\sqrt{2}}$.

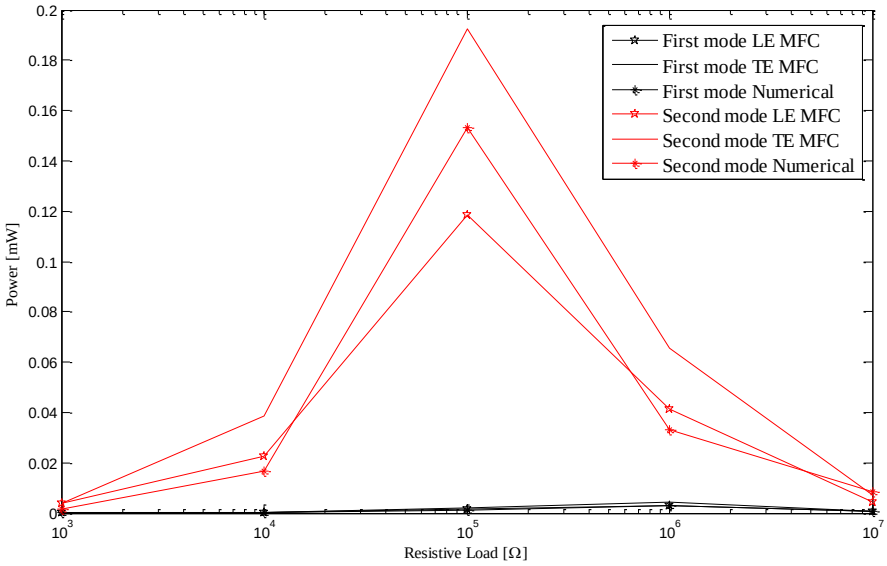

Figure 18: Power extracted from the wing modal excitation.
Experimental and numerical comparison.

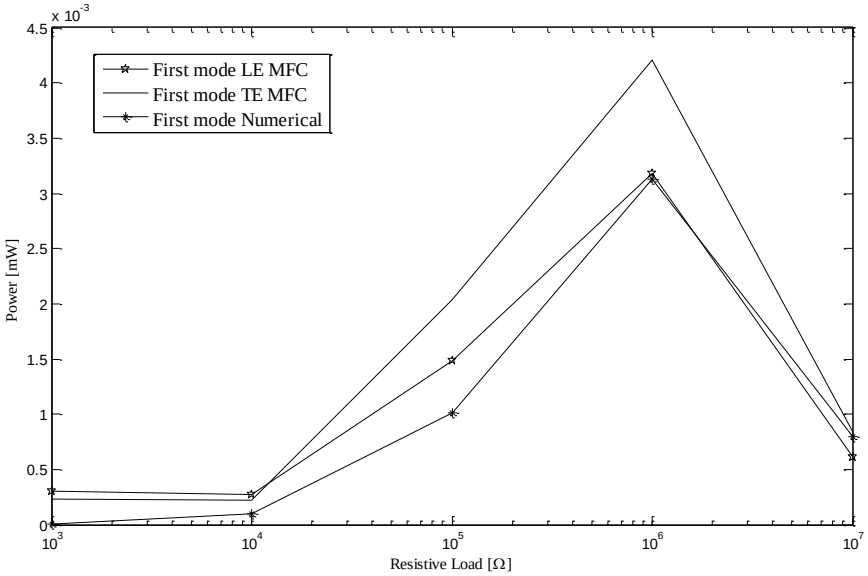

Figure 19: Detail of Figure 18. Experimental and numerical comparison.

From figures 18 and 19 it is reasonable to conclude that the results obtained from the numerical simulations are quite satisfactory if compared with the experimental once. The peak of power is coherently displayed at $10^6\ \Omega$ for the first mode and $10^5\ \Omega$ for the second, highlighting the importance of a tunable shunting circuit when the wing is excited in a wide range of frequencies. The amplitude of the extracted power is of the order of 10^{-1} mW, when the wing is excited at a frequency close to its second bending mode proper frequency, while it is of the order of 10^{-3} mW when the excitation frequency approach the first bending mode proper frequency. The results, in terms of power extracted from modal excitation, are very sensitive to the position of the piezoelectric patches. Figure 20 shows how, if we move the patches towards the wing tip, is the contribution to the power extraction from the second mode to increase, while if we move to the wing root is the contribution of the first bending mode, which is increased.

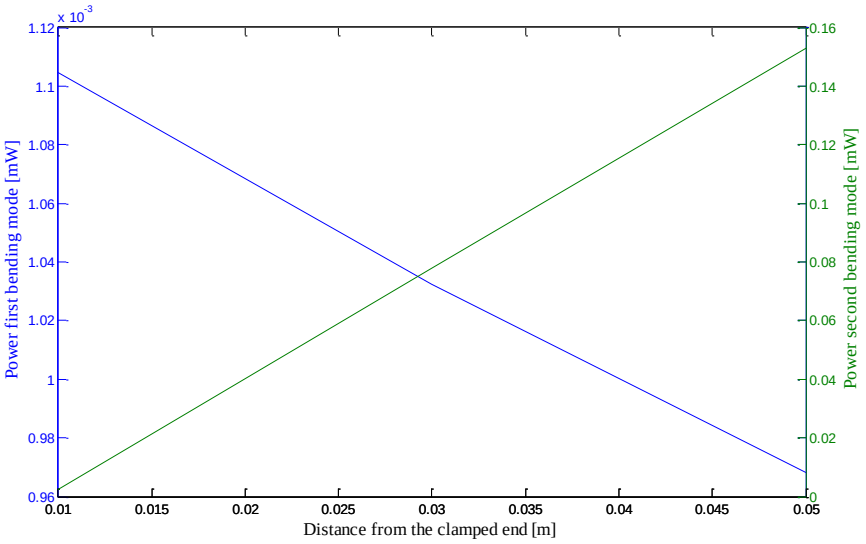

Figure 20: Power extracted from the first two bending mode
at R = $10^5\ \Omega$ vs. the piezo patches position.

The wing used in the WT tests, as mentioned in the previous section and at the beginning of this one, differs from that used in the modal testing for its length, which is in now 0.35 m, instead of 0.40 m, and without the solid clamping section. The piezoelectric patches location now starts from the clamped end of the wing. As In the WT tests the piezoelectric patches are connected to two equivalent resistive circuits and the output voltage is read by an oscilloscope, as in Figure 17. The experimental tests were performed by progressively increasing the flow speed in the testing chamber from 5 m/s to 30 m/s. The tests indicate that when the piezo patches are not connected to any electric circuit the flutter speed is found at about 27m/s where the amplitude of oscillation experiences and an abrupt jump in magnitude. However, when the patches are connected to a resistive electric circuit, the oscillation amplitude increase gradually. Figure 21 shows the root mean square of the wing tip oscillation amplitude vs. the air speed. The red curves refer to the numerical results while the black curves to the experimental results. The numerical wing has an open circuit critical flutter speed which is higher than the experimental one: 32.18 m/s circa. The difference in the critical flutter speed, may be explained by the fact that the two models are similar but not

exactly equivalents, the oscillation amplitude, between the experimental and the numerical models, is pretty comparable.

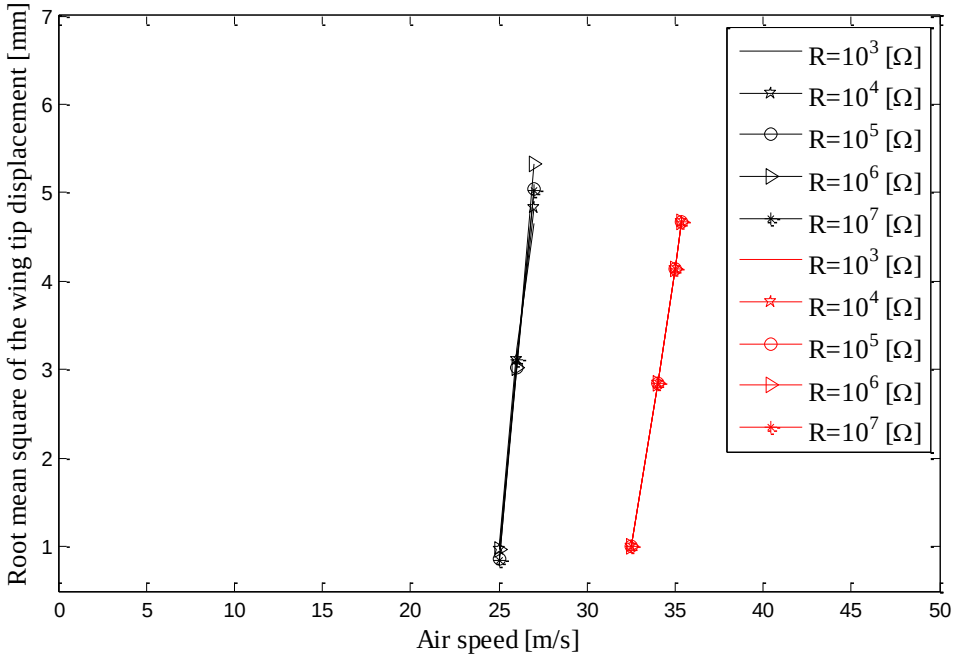

Figure 21: Wing tip displacement comparison between the experimental (black curves) and the numerical (red curves) wing.

The power extracted during the wind tunnel tests from flutter oscillations are reported in Figure 22, which refer to the LE electric circuit only.

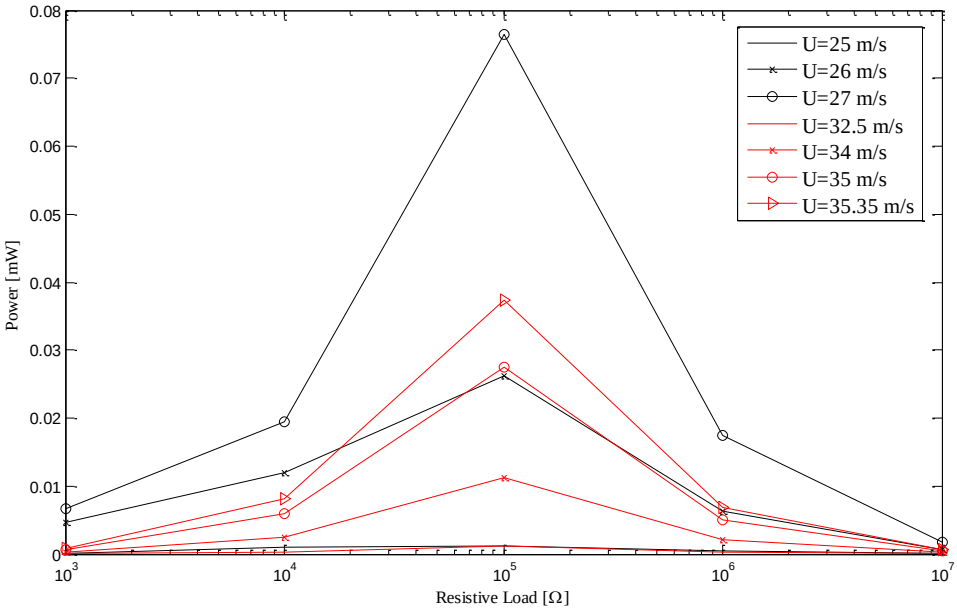

Figure 22: Comparison of the power output obtained from the LE electric circuit (black curves) and the numerical results (red curves).

Figure 22 shows that the numerically estimated and experimentally measured power are similar but with noticeable differences. This may be due to multiple reasons including the correct positioning of the piezo patches over the wing, the small difference between experimental and numerical oscillation amplitude, and the initial approximations made to develop the analytical model. It is important to consider the fact that the numerical model is not the exact representation of the experimental model and that the purpose of the investigation was not only to validate the numerical representation of the harvester but also to exploit the experimental results in order to performs some dedicated studies on the driving parameters and configurations in a piezoelectric harvesting process. The amount of power showed in Figure 22 refers to a single piezo patch; the LE patch for the experimental wing, while any of the two patches for the numerical wing. This means that the real instantaneous power, that this piezoelectric wing is able to provide to the global energy system, for the way it is designed, is the double of the value displayed in Figure 22. A power amount of the order of 1 mW is even more than the energy demand of MEMS technology and therefore it is worth, with a large margin of improvements, to be considered as an option for additional power on-board of the HALE aircrafts.

4. CONCLUSIONS

The widespread interest in developing new autonomous aircrafts that can perform long duration missions, on the order of the months, has motivated many studies on the design optimization of UAV. The goal of this manuscript it's to examine the challenges in using kinetic energy from structural vibrations to recharge on-board energy stores. Energy extraction from vibrations is not a new concept and is already used in urban infrastructure for both concurrent structural damping and energy scavenging, in the past, this has been infeasible for aerospace applications. In aerospace applications limit cycle oscillations due to flutter, is a favourable phenomenon to exploit for energy harvesting; it provides a constant oscillation in time and amplitude, at a given air speed and is examined in this present work. However, for structural safety reasons, it is not possible to rely on this as the only source of vibration on board. Using both frequency sweeps and wind tunnel tests performed on the frame, it was possible to qualitatively compare a numerical model of the piezoelectric harvester with experimental results. The results illustrate the importance of the piezoelectric patches location on the wing's dynamical response. What was seen is that the amount of energy extractable from the second bending mode of the wing is higher than that extractable from the first bending mode and it increases if the piezo patches are slightly moved towards the wing center. This suggest the necessity to develop a piezoelectric wing with multiple piezoelectric patches properly located in order to extract energy from the higher number of modes, or simply to the most excited mode, according to the good knowledge of the operational wing dynamic behaviour. The WT tests show that the order of magnitude of the energy extractable from LCOs/Flutter is of the order of 10 mW, a good result if compared to power demand many modern electronic devices.

5. REFERENCES

[1] Nickol, C. L., Guynn, M. D., Kohout, L. L., & Ozoroski, T. A. (2007). High altitude long endurance air vehicle analysis of alternatives and technology requirements development. AIAA Paper, 1050, 2007.

[2] De Marqui, C., Vieira, W. G., Erturk, A., & Inman, D. J. (2011). Modeling and analysis of piezoelectric energy harvesting from aeroelastic vibrations using the doublet-lattice method. *Journal of Vibration and Acoustics*, 133(1), 011003.

[3] Bryant, M., & Garcia, E. (2011). Modeling and testing of a novel aeroelastic flutter energy harvester. *Journal of vibration and acoustics*, 133(1), 011010.

[4] Akaydin, H. D., Elvin, N., & Andreopoulos, Y. (2010). Energy harvesting from highly unsteady fluid flows using piezoelectric materials. *Journal of Intelligent Material Systems and Structures*, 21(13), 1263-1278.

[5] Abdelkefi, A., Hajj, M. R., & Nayfeh, A. H. (2012). Piezoelectric energy harvesting from transverse galloping of bluff bodies. *Smart Materials and Structures*, 22(1), 015014.

[6] Júnior, C. D. M., & Maria, M. J. EFFECT OF PIEZOELECTRIC ENERGY HARVESTING ON THE RESPONSE OF A GENERATOR WING TO A TURBULENCE GUST.

[7] Bryant, M., & Garcia, E. (2009, March). Development of an aeroelastic vibration power harvester. In SPIE Smart Structures and Materials + Nondestructive Evaluation and Health Monitoring (pp. 728812-728812). *International Society for Optics and Photonics*.

[8] Nayfeh, A. H. and Pai, P. F. *Linear and non-linear structural mechanics*, 2004 (Wiley Interscience, New York)

[9] Crespo Da Silva, M., R., M., Glynn, C., C., "Nonlinear Flexural-Flexural-Torsional Dynamic of Inextensional Beam", 1986, *Journal of structural mechanics*, Volume 6 Issue 4.

[10] Kim, K., Nonlinear Aeroelastic Analysis of Aircraft Wing-With-Store Configurations, 2004, Ph.D thesis.

[11] Pai, P., F., "Three Geometrically Exact Beam Theories for Analysis of Highly Flexible 1-D Structures", 2011, 52nd AIAA/ASME/ASCE/AHS/ASC Structures, Structural Dynamics and Materials Conference, 4-7 April 2011, Denver, Colorado.

[12] Wagner, H., " Über die Entstehung des dynamischen Auftriebes von Tragflügeln ", Berlin: VDI-Verl., 1925.

[13] Shams, Sh., Haddadpour, H., Sadr Lahidjani, M. H., Kheiri, M., "An Analytical Method in Computational Aeroelasticity Based on Wagner Function", 2006, 25th International congress of the aeronautical sciences, ICAS 2006.

[14] C. Bruni, "ANALYSIS OF SLENDER PIEZOELECTRIC WING CONFIGURATIONS FOR ENERGY HARVESTING: AEROELASTIC MODELING AND EXPERIMENTAL COMPARISONS", 2016, Ph.D. Thesis.

[15] Bruni, Claudia, et al. "Energy harvesting from aeroelastic vibrations induced by discrete gust loads", *Journal of Intelligent Material Systems and Structures* (2016): 1045389X16642533.

[16] Bisplinghoff, R., Ashley, H., Halfman, R., *Aeroelasticity*, Dover 1996.

[17] Micro Fiber Composites - MFC. www.smart-materilas.com

[18] Ewins, D.J., Modal Testing: *Theory and Practice*, JOHN WILELY& SONS INC, 1984.

[19] *Fundamental of modal testing, Agilent Technologies*, Application note 243-3.

[20] Bruni C.; Cestino E.; Frulla G.; Marzocca P. (2014),Development of an Aeroelastic Wing model with piezoelectric elements for gust load alleviation and Energy Harvesting. In: ASME-2014, International Mechanical Engineering, Montreal (Canada), 14-20 November 2014.

[21] Bruni C.; Cestino E.; Frulla G. (2016), Parametric analysis of a fluttering piezoelectric wing. In: *AIRCRAFT ENGINEERING AND AEROSPACE TECHNOLOGY*, vol. 88 n. 3, pp. 382-388. - ISSN 1748-8842

[22] Bruni C.,Cestino E., Frulla G. (2013) Piezo-Aeroelastic modeling and flutter prediction of flexible composite wings. In: 8th International Conference "Supply on the Wings", Frankfurt, Germany, 5-7-November 2013.

ACKOWLEDGEMENTS

This research was supported by a financial grant from the A2-Net-Team project. We thank Clarkson University for having hosted us during the experimental test campaign and for providing expertise that greatly assisted the research.

COPYRIGHT STATEMENT